Heliyon 9 (2023) e21040

Contents lists available at ScienceDirect

Heliyon

journal homepage: www.cell.com/heliyon

Color properties and non-covalent interactions in hydrated (Z)-4-(1-cyano-2-(2,4,5-trimethoxyphenyl)-vinyl)pyridin-1-ium chloride salt: Insights from experimental and theoretical studies

Enrique Pérez-Gutiérrez [a], Atazaz Ahsin [b,c], Youness El Bakri [d,**], Perumal Venkatesan [a,e], S. Thamotharan [f], M. Judith Percino [a,*]

[a] Unidad de Polímeros y Electrónica Orgánica, Instituto de Ciencias, Benemérita Universidad Autónoma de Puebla, Val3, Eco-campus Valsequillo, Independencia O2 Sur 50, San Pedro Zacachimalpa, Pue. Mexico
[b] Beijing National Laboratory for Molecular Sciences, Institute of Chemistry, Chinese Academy of Sciences, Beijing 100190, China
[c] School of chemical sciences, University of Chinese Academy of Sciences, Beijing 100049, China
[d] Department of Theoretical and Applied Chemistry, South Ural State University, Lenin prospect 76, Chelyabinsk, 454080, Russian Federation
[e] Department of Chemistry, Srimad Andavan Arts and Science College (Autonomous), T.V. Koil, Tiruchirappalli 620 005, India
[f] Biomolecular Crystallography Laboratory, Department of Bioinformatics, School of Chemical and Biotechnology, SASTRA Deemed University, Thanjavur 613 401, India

ARTICLE INFO

Keywords:
Non-covalent interactions
Charge transfer
Pyridinium-quaternary salts
Spectroscopic characterization
computational methods

ABSTRACT

The optical charge-transfer (CT) property and the crystal structure of (Z)-4-(1-cyano-2-(2,4,5-trimethoxyphenyl)vinyl)pyridin-1-ium chloride monohydrate salt (**I**), which belongs to an acrylonitrile family, was studied. The title salt, **I**, was characterized using different spectroscopy techniques and a single-crystal X-ray diffraction study combined with quantum chemical computations. The results showed that the color properties of **I** are determined by the CT, changes in bandgap, optical absorption, and various non-covalent interactions. The HOMO-LUMO energy gaps are 5.41 eV and 5.23 eV for the precursor and salt, respectively. It was demonstrated that π-π stacking interactions lead to the formation of intercalated dimers and donor-acceptor interactions assisted by hydrogen bonds; the dimers and interactions are different between the precursor and the salt. The cation moiety is mainly stabilized by $N(1)^{+}$-H···Cl, and the anion is predominantly stabilized by strong O(1W)– H··· Cl^{-} bonds as well as the hydrogen bonds with the MeO group O(2W)–H···O(1) and O(2W)–H···O(1W). The charge transfer between cation and anion moieties in the structure is established through NBO analysis.

1. Introduction

Push-pull (donor-π-acceptor, D-π-A) molecules with pyridine moieties have been of great interest for many applications in optoelectronics, material science, and bioactive molecules due to their unique properties, such as aromatic character, high dipolar nature, and electronegative nitrogen atoms present in the phenyl ring. Pyridine derivatives extend their conjugations through the π-electron system with various donor units (D, i.e., aromatic or conjugated molecules), and the pyridine nitrogen atom acts as an electron

* Corresponding author
** Corresponding author
E-mail addresses: yns.elbakri@gmail.com (Y. El Bakri), judith.percino@correo.buap.mx (M.J. Percino).

https://doi.org/10.1016/j.heliyon.2023.e21040
Received 22 May 2023; Received in revised form 9 October 2023; Accepted 13 October 2023
Available online 18 October 2023
2405-8440/© 2023 The Authors. Published by Elsevier Ltd. This is an open access article under the CC BY-NC-ND license (http://creativecommons.org/licenses/by-nc-nd/4.0/).

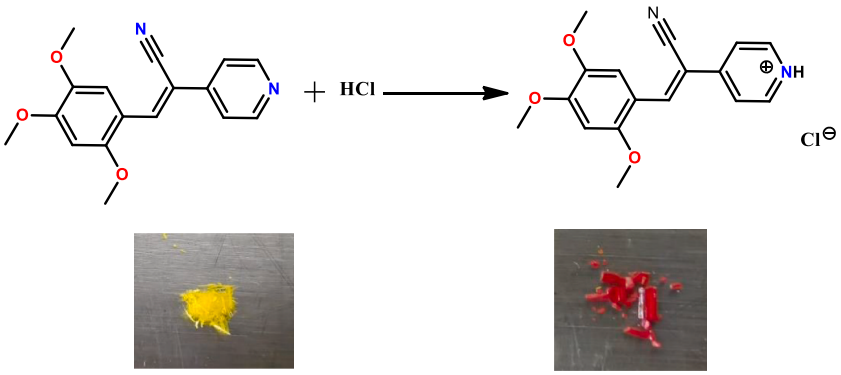

Scheme 1. Synthesis of (**I**) and color after salt formation.

acceptor (A) of the corresponding donor molecules [1,2]. The optical and electrochemical properties of different series of organic D-π-A molecules have been studied [3]. The modification of the electron acceptor or donor units in the push-pull molecules has been tuned for their absorption and emission properties [3]. Mainly, the strong bathochromic shift of absorption and emission of the new push-pull dye molecules has been achieved by the modification of the donor, acceptor, and π conjugation units through the lowering of the energy gap between the highest occupied molecular orbital (HOMO) and the lowest unoccupied molecular orbital [4,5]. Based on the tunable property of the push-pull molecules, they have been used as ON-OFF switches, ion sensing materials, and other applications. These push-pull molecules are also sensitive to external stimuli such as temperature, polarity, viscosity, pH, and crystal packing [3,6–9]. Among the various kinds of push-pull molecules, stilbazolium (D-π-A^+ X^-) based salts exhibit many interesting optical and optoelectronic properties, which have been extensively studied [10–14]. For example, some stilbazolium salts were used as fluorescence probes to monitor free radical polymerization processes and viscosity changes [15–17]. Additionally, the first commercial stilbazolium-based second-order nonlinear optical material, DAST (4-(N,N-dimethylamino)-N-methyl-4-stilbazolium tosylate), was reported in 1989 by Marder et al. [14,18]. Recently, 4-(N,N-dimethylamino)-N-methyl-4-stilbazolium with different anions, such as *p*-hydroxy benzenesulfonate, *p*-aminobenzenesulfonate or *p*-dimethylaminobenzene sulfonate, was also synthesized, and its nonlinear optical (NLO) properties were explored [19–22]. Considering the potential importance of push-pull molecules, various ionic push-pull compounds, such as hemicyanine dye, indolinium, benzothiazolium, benzooxazolium, benzoimidazolium, pyridinium, quinolinium and Schiff bases molecules, have been explored in the last few decades [23–25].

As mentioned earlier, these classes of compounds have a positive charge on the ring nitrogen atom that acts as a strong electron acceptor, and it enhances conjugation from various functional terminals in the aromatic donor (D) part. Solvatochromism, acidochromism, the effect of protonation [26–28], and the photophysical behaviors of this class of compounds have been studied [29]. Based on the wide range of requirements for new organic push-pull molecules with large second-order nonlinearity, optical polarizability is one of the most critical requirements for modern photonics [30]. On the other hand, synthesizing organic molecules with long emission (i.e., red and NIR regions) and a high fluorescence quantum yield is very attractive. Red and NIR dyes are widely used in fluorescent probes, immunostaining, immunohistochemistry, and biochemistry for optical imaging and analytical sensing [31]. The charge-transfer process of the D-π-A molecules with a small bandgap achieved longer wavelength emission [32]. Since most "push–pull'' chromophores are organic molecules, with donor-π-conjugated system-acceptor (D-π-A), these three key components can vary widely to achieve their tailor-made optical and optoelectronic properties [33–35]. Among them, the α, β acrylonitriles or α-cyanostilbene derivatives also exhibit significant solvatochromic emission behavior and have similar enhanced emission characteristics in water and the solid-state [36,37]. The intermolecular and intramolecular interactions of these π-conjugated systems largely contribute to their excellent photophysical properties as charge-transfer characteristics were explored [37]. Briefly, the existence of charge transfer between cation and anion moieties in the 1-allyl-4-(1-cyano-2-(4-dialkylaminophenyl)vinyl)pyridin-1-ium bromide salts and their strong bathochromic shift on the absorption in solution and solid-state were explored. Additionally, the charge transfer of the molecules was enhanced by the quaternised pyridine nitrogen and counter bromide ion, and it yielded strong bathochromic shift molecules when compared with nonquaternised molecules (i.e., (Z)-3-[4-(dialkylamino)phenyl]-2-(4-pyridyl) prop-2-enenitrile). Based on earlier studies, quaternization or pH changes tune the optical properties of this class of molecules. Hence, these molecules may be used to monitor changes in pH in environmental samples or are important in industrial and health care applications. This has led to an important shift toward developing photoresponsive chemosensors. Continuing our interest in the structure-optical properties of α,β-acrylonitrile crystals with different moieties, we explored their intermolecular non-covalent interactions in their solid-state [38–41]. In the present investigation, a charge-transfer salt hydrate was prepared. Although the color changes are known experimentally when a base (pyridine) is neutralized with 1 M HCl, the formed salts were isolated and characterized. Herein, the physical properties of the title salt, crystal structure, and crystal packing were analyzed with the aid of experiments and various theoretical tools. Furthermore, DFT computational calculations were carried out to better approximate the experimental data.

2. Experimental

2.1. Synthesis of (Z)-4-(1-cyano-2-(2,4,5-trimethoxyphenyl)vinyl)pyridin-1-ium chloride (I)

(**I**) was synthesized with 50 mg of (Z)-3-(2,4,5-trimethoxyphenyl)-2-(pyridin-4-yl)acrylonitrile [OPUSEA] with drops of 1 M HCl solution (Scheme 1). The solution instantly changed from yellow to dark red, and a red precipitate was formed after a few minutes. Ten milligrams of **I** red solid was dissolved in 10.0 mL of ethanol; the red solution was evaporated at room temperature. After 48 h, crystals were formed in the form of red rectangular prisms with a melting point of 218–220 °C. The reaction between the precursor and acid vapor also achieves salt formation.

2.2. Instrumentation

Melting points were measured with the SEV (0–300 °C) apparatus and were reported as uncorrected values. IR spectra of the products were recorded on a Vertex (Model 70, Bruker Optics, Germany) 750 FT-IR spectrophotometer by attenuated total reflectance (ATR) using KBr as the substrate. ^{1}H NMR and ^{13}C NMR spectra were obtained in DMSO-d_6 on a Bruker 500 MHz NMR spectrometer (Varian NMR, Walnut Creek, CA). The electron ionization (EI-MS) spectrum was acquired on a Jeol MStation 700-D mass spectrometer (Jeol USA, Peabody, MA). The absorbance spectra (UV–Vis) were acquired with a Cary 300 spectrometer (Agilent Technologies Inc.)

2.3. Single crystal X-ray diffraction (SCXRD)

All reflection intensities were measured at 110(2) K using a SuperNova diffractometer (equipped with an Atlas detector) with Cu $K\alpha$ radiation (λ = 1.54178 Å) under the program CrysAlisPro (Version CrysAlisPro 1.171.39.29c, Rigaku OD, 2017) [42]. The same program was used to refine the cell dimensions and to reduce data. The structure was solved with the program SHELXS-2018/3 (Sheldrick, 2018) and was refined on F^2 with SHELXL-2018/3 [43]. Analytical numeric absorption correction using a multifaceted crystal model was applied using CrysAlisPro. The data collection temperature was controlled using the Cryojet system (manufactured by Oxford Instruments). The H atoms were placed at calculated positions (unless otherwise specified) using the instructions AFIX 43 or AFIX 137 with isotropic displacement parameters having values of 1.2 or 1.5 U_{eq} of the attached C atoms. The H atoms attached to the N1, O1W, and O2W were found from different Fourier maps. Their coordinates were restrained pseudo-freely using the DFIX instruction to keep the N–H, O–H, and H···H distances within acceptable ranges. The structure is ordered.

2.4. Computational methodology

One of the most pertinent aspects of density functional theory (DFT) is how well it can be employed to define and elucidate fundamental chemical concepts such as molecule structure and reactivity. In this study, the compound created by the G09 software is theoretically investigated using density functional theory (DFT) [44]. The depiction of the geometries was obtained using GaussView 5.0 and IQ-mol software. The entire quantum chemical simulations for the studied liquid crystal are performed at the m06-2x in conjunction with the def2-TZVP basis set. The adopted M06-2X functional is a high-nonlocality functional with double the amount of nonlocal exchange (2X) [43]. This functional is recommended and well presented to study properties like thermochemistry, kinetics, noncovalent interactions, and electronic excitation energies to valence and Rydberg states [44,45]. The choice of basis set is also crucial for quantitatively determining physio-chemical properties. Therefore, we adopted the second-generation default (def2) Karlsruhe basis set with triple valence polarized (def2-TZVP) [46]. Furthermore, we have considered an implicit solvent model using SDM with ethanol [47]. The frequency calculations are performed using the same method to confirm the stability of the structure. We calculated the ionization potential (IP) and electron affinity (EA) of the synthesized liquid crystals to determine their electronic stability and reactivity. Orbital and natural bonding orbital analysis is used to investigate the nature of bonding and reactivity of crystals.

To determine the conductivity and reactivity of the compound, we also conducted a density of states (DOS) analysis using GaussSum software. Moreover, we estimated the optical and nonlinear optical characteristics of the compounds using the same theoretical approach. For optical and NLO properties, the dipole moments (μ_o), polarizability (α_o), polarizability volume, hyperpolarizability (β_o), and projection of hyperpolarizability on the dipole moment vector are determined using the same method.

We also carried out Hirshfeld analysis to visualize intermolecular interactions in the crystalline state and to explore the spatial location of contact between different fragments of the molecule. This analysis is carried out using the crystal explorer program package. To visualize the interaction topology in these crystal structures, energy framework analysis was performed using Crystal Explorer [48,49]. Topological parameters for non-covalent interactions at their critical bond points (BCPs) were calculated based on Bader's Quantum Theory of Atoms in Molecules (QTAIM) framework. With the AIMALL program [50], the topology results (BCP), electron density $\rho(r)$ in the BCP, Laplacian electron density $\nabla^2\rho(r)$, and the interaction of H and the acceptor atom were obtained. The bonding (rD and rA) and nonbonding radii of the donor (roD) and acceptor (roA) atoms are compared. The bond radii are taken as the length from the BCP to the nuclei, while the radii of unbonded hydrogen and acceptor atoms are taken as the van der Waals radii in the gas phase [51]. The graph of the molecule's contour of the intramolecular interactions was used with the function Rho, electron density, and the Laplacian of the Electron Density, DelSqRho, function with a resolution of 0.05. The NCI (Non-covalent Interaction) graphs were made with the function |RDG|: Magnitude of the reduced electron density gradient with isosurfaces = 0.5, Map function: Sign (HessianRho_EigVal_2)*Rho and a maximum electron density of 0.7.

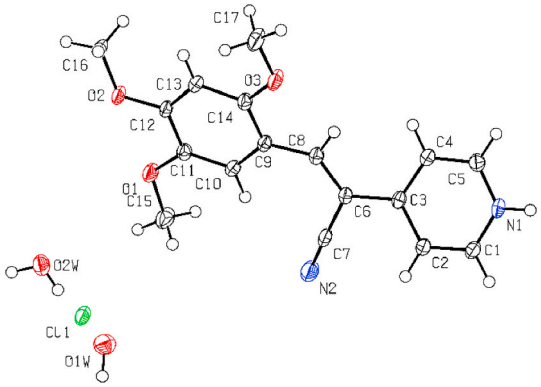

Fig. 1. ORTEP view of protonated salt **I** with a displacement ellipsoid plot (50 % probability level) at 110 K.

Table 1
Select bond lengths (Å) for the molecular structures of precursor [OPUSEA] and **I**.

Trimethoxy phenyl				
Assigned [54]	Precursor [52]		I	
Bond $C_{ar} \approx C_{ar}$	C(9)–C(10)	1.405(4)	C(9)–C(14)	1.4127(16)
C ≈ C (overall)	C(10)–C(11)	1.402(3)	C(13)–C(14)	1.3953(15)
1.380	C(11)–C(12)	1.383(4)	C((13)-C(12)	1.3821(17)
1.384	C(12)–C(13)	1.411(4)	C(12)–C(11)	1.4135(16) 1.3738(16)
	C(13)–C (14)	1.376(3)	C(11)–C(10)	1.4134(17
	C(9)–C(14)	1.404(4))	C(10)–C(9)	
C_{sp3}-O(2)	C(15)–O(1)	1.434(3)	C(17)–O(3)	1.4259(16)
CH–*O*-C_{ar}	C(16)–O(2)	1.428(3)	C(16)–O(2)	1.4403(14)
	C(17)–O(3)	1.428(3)	C(15)–O(1)	1.4287(15)
Acrylonitrile moiety				
Double bond $C_{sp2} = C_{sp2}$ (overall)1.316[a]with Ar. 1.339	C(6)–C(8)	1.358(3)	C(6)–C(8)	1.3608(16)
C_{sp2}-C_{ar} (overall) 1.483;	C(5)–C(6)	1.486(3)	C(3)–C(6)	1.4759(15)
(conjugated) 1.470, 1.488	C(8)–C(9)	1.446(3)	C(8)–C(9)	1.4408(16)
Pyridine syn to CN				
C ≈ N (pyridine),	C(1)–C(5)	1.396(3)	C(2)–C(3)	1.4011(16)
1.337	C(4)–C(5)	1.390(3)	C(3)–C(4)	1.3994(17)
C–N^+-H (pyrimidinium)	C(1)–C(2)	1.384(4)	C(1)–C(2)	1.3734(16)
1.335	C(3)–C(4)	1.388(4)	C(4)–C(5)	1.3748(17)
$C_{ar} \approx C_{ar}$ in pyridine 1.380	C(2)–N(1)	1.336(4)	C(1)–N(1)	1.3399(16)
In pyridinium cation (N^+-H;	C(3)–N(1)	1.346(4)	C(5)–N(1)	1.3405(16)
C2–C3 1.373; C3–C4 1.383				

[a] When conjugated.

3. Results and discussion

3.1. Spectroscopic characterization of salt I

Title salt **I** was characterized by FT-IR, ^{1}H, ^{13}C NMR, and UV–Vis spectral analysis; these results are provided in the supporting information (ESI, Figs. S1–S3). To clearly understand the formation of the title salt, the HCl vapors were passed on to the precursor, and after some time, the color changed, which indicated the formation of protonated salt **I**. The experimental procedure for this conversion is described in the ESI, Fig. S2. The IR spectra of precursor and protonated title salt (red solid) **I** are shown in Fig. S1. As seen in Fig. S1, the absorption bands of **I** are different from those of the precursor, especially the band at 3573 cm^{-1}, the broad bands at 2840-2355 cm^{-1}, which correspond to νN^+-H of pyridinium salts (hydrogen-bonded, overlapping with the band of –CN) and the band at 1633 cm^{-1}, which is for the νC=C vibration of the pyridine ring; this provides evidence for the protonation of the precursor molecule. The effect of salt formation changed the nuclear environment, and the chemical shift of protons appeared downfield, which is an indication that the electron density is delocalized (Table S1 and Fig. S3).

3.2. Crystal structure analysis

The ORTEP view of the asymmetric unit of salt **I**, along with atom labeling, is shown in Fig. 1. The asymmetric unit of **I** consists of a cation and chloride anion along with two H_2O molecules. Crystal data and refinement statistics are summarized in Table S2. The geometrical parameters, such as bond length, bond angles, and torsion angles, are displayed in Tables S4–S5. Title salt **I** crystallized in

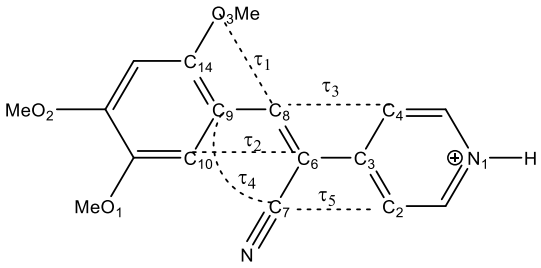

Scheme 2. Selected torsion angles for title salt (**I**).

Table 2
Selected torsion angle of the precursor [OPUSEA] and **I**.

Torsion angle	Precursor [30]	(θ, °)	I	(θ, °)
τ_1	C(8)-C(9)-C(10)-O(1)	3.6(3)	C(8)-C(9)-C(14)-O(3)	−5.78(16)
τ_2	C(6)-C(8)-C(9)-C(14)	7.1(4)	C(6)-C(8)-C(9)-C(10)	−9.8(2)
τ_3	C(4)-C(5)-C(6)-C(8)	13.2(4)	C(7)-C(6)-C(8)-C(9)	−4.4(2)
τ_4	C(7)-C(6)-C(8)-C(9)	3.6(4)	C(4)-C(3)-C(6)-C(8)	−23.67(17)
τ_5	C(1)-C(5)-C(6)-C(7)	11.8(3)	C(2)-C(3)-C(6)-C(7)	−20.08(16)

Table 3
Hydrogen bonds D ··· H ··· A (Å) and D−H ··· A angles (°) of **I**. ("Mercury 3.5.1. (accessed on December 13, 2023)).

Possible interactions	Geometry (Å,°)				Symmetry
	d(D—H)	*d*(H···A)	*d*(D···A)	∟D … H … A	
N1–H1N···Cl1	0.901 (15)	2.130 (15)	3.0302 (10)	176.6 (14)	x+1/2, −y+3/2, z+1/2
O1W–H1W1···Cl1	0.868 (16)	2.341 (16)	3.1985 (11)	169.8 (16)	x, y, z
O1W–H1W2···O2W	0.850 (16)	1.986 (17)	2.8343 (14)	176.2 (18)	−x+1/2, y−1/2, −z+1/2
O2W–H2W1···O1W	0.821 (16)	2.001 (16)	2.8182 (15)	173.1 (18)	x, y, z
O2W–H2W2···O1	0.843 (16)	2.142 (16)	2.9200 (13)	153.3 (16)	−x+1/2, −y+3/2, −z
O2W–H2W2···O2	0.843 (16)	2.497 (17)	3.1892 (13)	140.0 (15)	−x+1/2, −y+3/2, −z

the monoclinic system with *C*2/*c* with Z = 8. The precursor [OPUSEA] molecule crystallized in the monoclinic system with $P2_1$ and Z = 2 [52]. Furthermore, to understand the push-pull effect on the optical properties of **I** because of protonation on the precursor molecule, the bond lengths around the pyridine ring are compared (i.e., bond length variation around the pyridine ring is compared with precursor and protonated form, **I**). Similar bond length variations were observed earlier [37,53,54]. A significant difference in the bond lengths is observed between salt **I** and its precursor. Briefly, the C_{Ar}═C_{Ar} bond length in C(9) = C(14) and C(9) = C(10) in the trimethoxyphenyl group of **I** is longer, and C(13) = C(14) shorter than their precursor compound, Table 1. The bond lengths of the C_{Me}–O bonds in **I** are also varied (i.e., the bond lengths elongate in C(16)–O(2) and C(15)–O(1)). Strong bond shortening (C(1)–C(2) and C(4)–C(5)) and elongation of C_{Ar}═C/N_{Ar} are observed in the pyridinium ring of **I**. These bond length values are comparable with the pyridinium compounds reported by Allen [55]. Bond alternation in the title salt could indicate that there is a strong delocalization of the electronic density in specific parts of the molecular structure. It plays a significant role in altering the physicochemical properties of the molecule.

The selected torsion angles (τ, Scheme 2) in a title salt (**I**) are compared with its precursor compound; values are listed in Table 2. As seen in Table 2, the torsion angles in **I** are larger than their precursor. The molecular structure of the title salt is not planar. In contrast, the central acrylonitrile group and a pyridine ring in the precursor molecule were coplanar [52]. Particularly, when compared with the precursor molecule, a larger deviation of the torsion angle ($\tau_4 \approx 27^\circ$ and $\tau_5 \approx 32^\circ$) around the acrylonitrile group is observed in the title salt (**I**), which might be due to the quaternization of a pyridine nitrogen atom. Furthermore, this deviation was shown by the dihedral angle between two mean planes formed by the atoms in the pyridinium ring (plane: N1, C1–C5) and the acrylonitrile group (plane: N2, C7, C6, C8) is 22.15°. This rotation is favored for the additional intermolecular interaction in the title salt when compared with their precursor molecule [OPUSEA].

Various nonvalent interactions (NCIs) contribute to forming different molecular pairs or dimers, which are significantly involved in the stabilization of title salts. The hydrogen bond (HB) parameters for the different molecular pairs are listed in Table 3. As seen in Table 3, various kinds of HBs are observed. In brief, strong charge-assisted hydrogen bonds (N1–H1N···Cl1); strong HBs ($O1_W$–$H1_{W1}$···Cl1; $O1_W$–$H1_{W2}$···$O2_W$); and moderate and weak HBs (O2W–H2W2···O1/O2) formed between the –OCH_3 group are observed, and this classification is based on Jeffrey [56,57]. Apart from these classical intermolecular interactions, the π ··· π (π stacking) interaction seemed between the pyridinium and the aromatic rings was present. It should be mentioned that this π stacking interaction is somewhat different from that in the precursor. The parallel π stacking interaction (i.e., π stacking interaction between

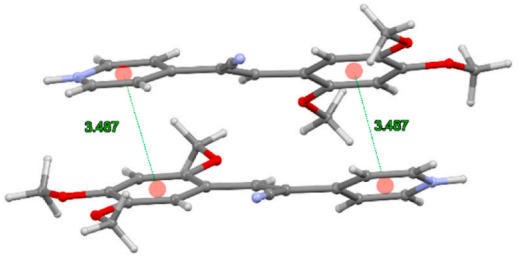

Fig. 2. An anti-parallel π stacking interaction between two opposite-arranged molecules.

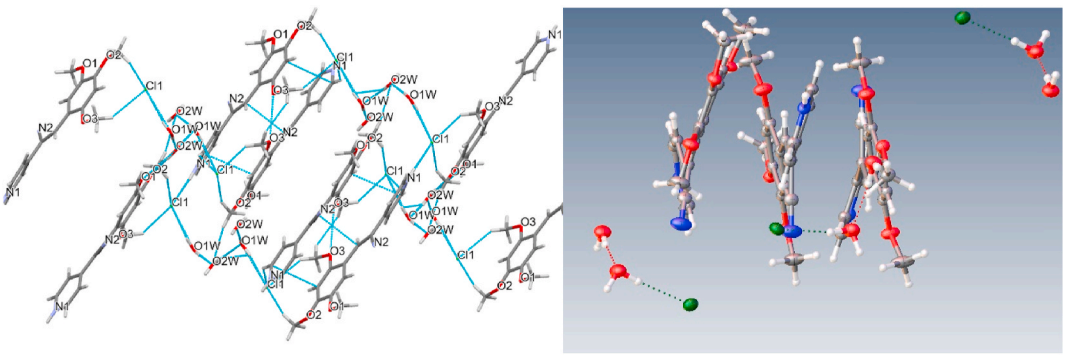

Fig. 3. Crystal packing diagram of **I** and perspective view of the molecular structures showing weak π–π interactions and hydrogen bonds (Dolomanov et al., 2009; "Mercury 3.5.1. (accessed on December 13, 2023)).

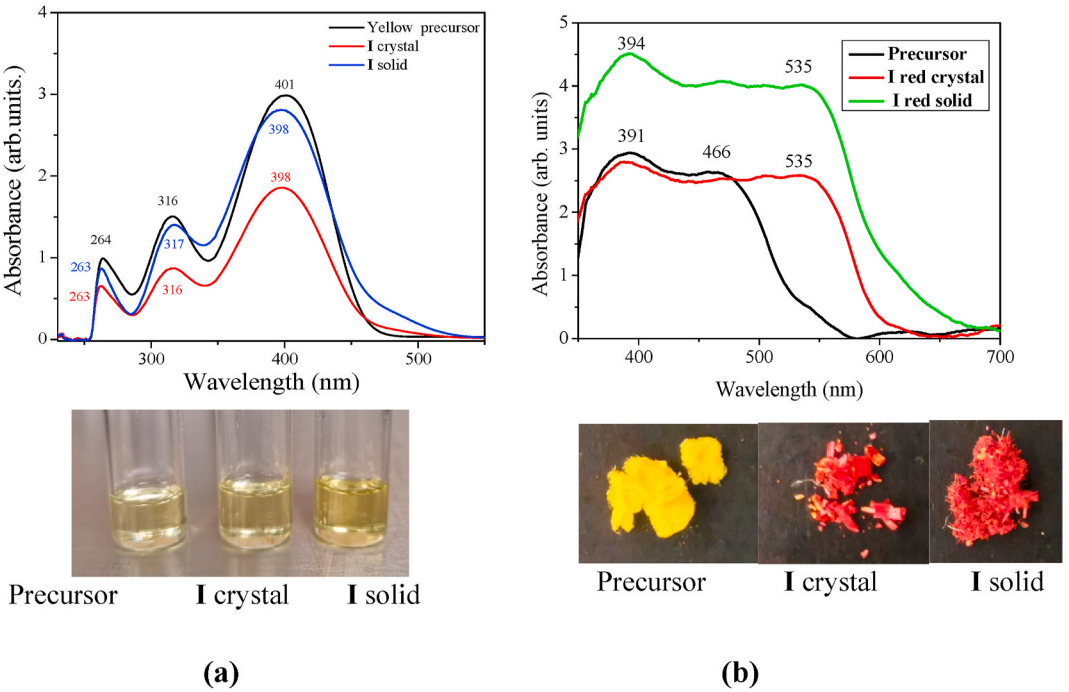

Fig. 4. Absorption spectra of **I** and the precursor compound in DMSO and in the solid state.

two trimethoxyphenyl rings) occurred in two adjacent precursor molecules with centroid to centroid distance (Cg ··· Cg) being 3.920 Å. However, anti-parallel π stacking interaction (i.e., π stacking interaction between the pyridinium ring and a trimethoxyphenyl ring) occurred between two adjacent molecules of the title salt centroid to centroid (Cg ··· Cg) distance being 3.487 Å, which is 0.433 Å

Table 4
Second order perturbation theory analysis of Fock matrix for studied salt on NBO basis.

Donor (i)	Acceptor (j)	E(2) kcal/mol	E(*j*)-E(i) au	F(i,j) au
π(C1–C3)	LP*(C5)	76.13	0.19	0.125
π(C6–C8)	LP*(1) C5	76.58	0.19	0.125
π(C18–C19)	LP*(1) C21	80.40	0.18	0.129
LP(O38)	σ*(C18–C19)	10.11	1.24	0.100
LP (O38)	π*(C18–C19)	44.51	0.44	0.132
LP (O39)	LP*(1) C21	67.29	0.27	0.152
π(C10–C12)	π*(C11–N36	14.84	0.087	0.09
BD*(3)C11–N36	π*(C10–C12)	7.17	0.48	0.055
π(C18–C19)	π*(C15–C17)	18.20	0.02	0.091
π(C15–C17)	π*(C18–C19)	29.93	0.35	0.095
π(C10–C12)	π*(C10–C12)	1.62	0.40	0.023
π(C10–C12)	LP*(1) C5	38.16	0.20	0.097
LP (O39)	σ*(C30–H33)	6.59	0.82	0.068
σ(N35–H35)	σ*(C6–C8)	3.88	1.35	0.065
σ(N34–H35)	σ*(C1–C3)	3.44	1.35	0.061
π(C10–C12)	LP(C14)	19.43	0.20	0.077
π(C1–C3)	π*(C1–C3)	0.94	0.36	0.017

Table 5
Computed electronic properties and reactivity descriptors. The point group symmetry, electronic energy (in Hartrees), dipole moment (μ in Debye), HOMO and LUMO energy (in eV), HOMO-LUMO gap ($E_{H\text{-}L}$ in eV), ionization potential (IP in eV), electron affinity (in eV), chemical hardness (Η in eV), partial NBO charges on the atom (QX in |e|), chemical potential (μ in eV), electronegativity (χ in eV), electrophilicity index (ω in eV), polarizability (α_o in au), hyperpolarizability (β_o in au), and polarizability volume (α_v in $Å^3$) of the liquid crystal.

Solvent = Ethanol	
Symmetry	C_1
Total electronic energy	−1606.32
Interaction energy (E_{int})	−86.80
Q(N/O/Cl)	−0.46/-0.81/-0.64
Dipole moment (μ_o)	17.88
HOMO	−7.19
LUMO	−1.96
HOMO-LUMO gap ($E_{H\text{-}L}$)	5.51
Ionization potential (IP)	7.19
Electron affinity (EA)	1.96
Chemical hardness (Η)	2.61
Chemical potential (μ)	−4.57
Electronegativity (χ)	4.57
Electrophilicity index (ω)	4.14
Polarizability (α_o)	408.43
Polarizability volume (α_v)	48.055
Hyperpolarizability (β_o)	18837.03

shorter than that in the precursor molecule [52], and this Cg ··· Cg distance falls in the typical stacking interaction range (<4.00 Å and offsets of 1.6–1.8 Å) [58]. The face-to-face manner of the molecular arrangements is observed in this anti-parallel π stacking interaction (Fig. 2). This is significantly involved in stabilizing the title salt (Fig. 3), and these π stacking interactions enhanced the charge transport property of the title salt. The improved charge transport property of **I** might be due to the change in the optical property (such as the color, absorption, and emission) compared with the precursor molecule [52]. The change in color owing to intermolecular interactions have been reports for some complex [59,60].

3.3. Optical properties of *I*

The UV–vis absorption spectra of **I** and its precursor were recorded in DMSO at a concentration of 1 mM and room temperature (Fig. 4). Fig. 4a shows no significant difference in the absorbance wavelengths in solution for the precursor, amorphous powder (red solid), and red crystal of **I**. The absorption spectra showed three absorbances, the first (λ_{max}) at 396 nm with the highest intensity and the second and third absorbances at 316 and 263 nm, respectively. In brief, all the above three absorbances in **I** and their precursor are the typical n→π* and π→π* transitions, and no bathochromic shift is seen in the solution state. In contrast, a large bathochromic shift was observed in the λ_{max} between **I** and its precursor in the solid-state UV–vis absorption spectra (Fig. 4b). In outline, the solid-state

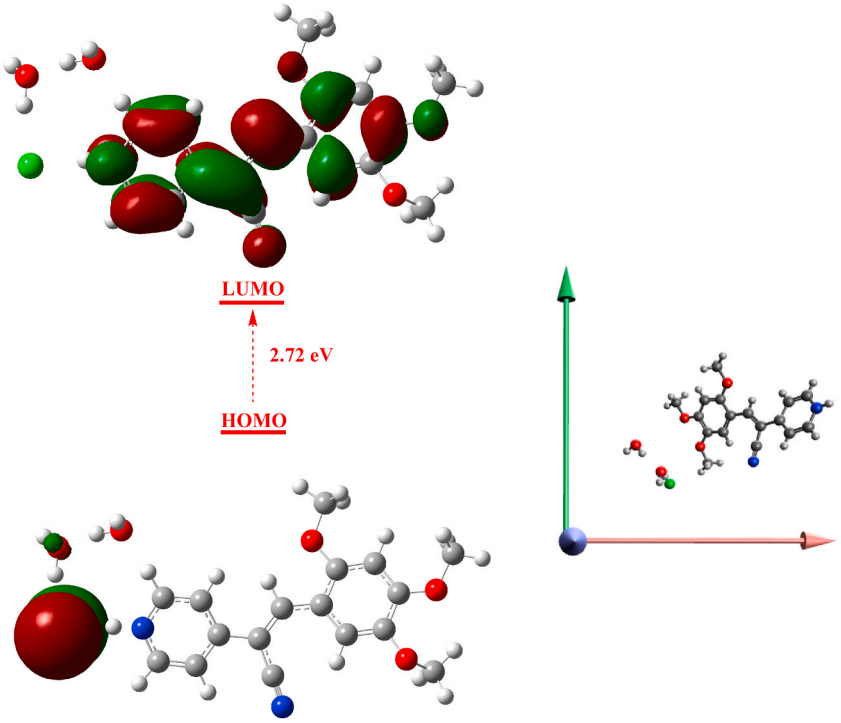

Fig. 5. Optimized geometry and HOMO-LUMO of the title salt, **I** at M06-2X/def2-TZVP.

λ_{max} for **I** is at 535 nm (both amorphous powder and red crystals) and at 466 nm for λ_{max} of the precursor. As stated earlier, a strong redshift (130 nm) absorption was observed between **I** and its precursor, which could be due to charge transfer between the molecules, and it is enhanced by strong charge-assisted hydrogen bonds and other non-covalent intermolecular interactions in pyridinium salt formation (**I**).

3.4. Theoretical study of I

3.4.1. Optimized geometries and stability of the crystal

The optimized geometry of the title salt **I** in SDM model using ethanol were obtained at M06-2X/def2-TZVP level of theory, and it has C1 point group symmetry. Computational methods based on implicit solvent models can be used to approximate thermodynamics and electronic properties. The central acrylonitrile group and a pyridinium ring optimized molecule are in the coplanar, whereas the $-OCH_3$ group substituted phenyl ring is rotated away from the planar structure. For determining the thermodynamic stability of compound, we calculated the interaction energy (E_{int}) given by:

$$E_{imt} = \left[E_{Complex} - \left(E_{H2O} - E_{Cl} - E_{Organic\ moitie}\right)\right] \quad (1)$$

The SDM model employed using ethanol as solvent. The obtained interaction energy of salt in ethanol solvent is −86.80 kcal/mol (Table 4). The negative value of E_{int} is suggesting its thermodynamic stability. The optimized and crystal structures are well overlaid with each other. The water molecules lie at the corner of the central fragment, along with the chloride ion. Furthermore, the absence of negative frequency in the vibrational analysis in our simulations suggests that the potential energy surface's geometry is truly minimal and implies that the surface does not belong to the saddle point. The optimized structure is used to calculate different parameters, i.e., dipole moment and the DFT global parameters. The calculated dipole moment (μ) value is 17.88 Debye (see Table 5), which is quite high and suggests asymmetric charge distribution in the molecular structure. The observed significant value of the dipole moment also suggests salt's polar nature, which enhances its reactivity.

3.4.2. Frontier molecular orbital (FMO) and natural bond orbital (NBO) analysis

Frontier molecular orbital (FMO) analysis is a quantum chemical tool used to describe the chemical reactivity and kinetic stability of molecules. FMO studies are recognized as important tools for understanding different properties of molecules, including optical characteristics, chromophore interactions, charge transfer properties, chemical stability, chemical reactivity, etc. The electron-accepting and electron-donating capacity of the title salt can be explained based on the lowest unoccupied molecular orbital (LUMO) and highest occupied molecular orbital (HOMO) energy levels. The HOMO of the title salt was localized on the chloride anion, whereas the LUMO was predominantly localized on the cationic part of the whole molecule. The pictorial representations of HOMO-LUMO densities are given in Fig. 5. The computed energy value for HOMO and LUMO is −7.19and −1.96, respectively (Table 5). The

energy gap ($E_{H\text{-}L}$) is found to be 5.23 eV, and this energy gap value is comparable to the precursor molecule ($E_{H\text{-}L}$: 5.41 eV, calculated at M062x/cc-pVTZ level of theory) [30]. The lowering of the energy gap of **I** indicates that the molecules in the soft nature enhanced the reactivity and intra-molecular charge transfer process.

Natural bond orbital (NBO) analysis was performed to understand the charge transfer properties of the title salt. The computed partial NBO charges on particular atoms are given in Table 4. The calculated NBO charge on the oxygen atom is −0.81 |e|, which is the highest in magnitude (negative). The obtained charges on oxygen atoms within the compound are negative, but the highest magnitude is found for oxygen of water molecules. Similarly, the negative NBO charges were calculated for nitrogen within the central ring, and the charge was transferred from hydrogen (electropositive) to carbon and nitrogen. A negative partial NBO charge (−0.64 |e|) can be seen on the Cl^{-} ion, which lies near water molecules, and the charge is transferred through non-covalent interactions.

Additionally, we interpreted the second order perturbation theory analysis of fock matrix to explain the concept of intra- and intermolecular interactions in studied compound. The values are given in Table 4. In this analysis, the interaction of between donor and acceptor electrons in with stabilization energy E(2). The higher stabilization energy reveals the most significant interactions due to pi-electrons (π), lone pair (LP), and sigma (σ) to their corresponding antibonding. One can notice the significant interaction of lone of electrons (nonbonding) with antibonding orbitals LP(O38) → π*(C18–C19), LP (O38) → π*(C18–C19), and LP (O39) → LP*(1) C21 with the stabilization energy of 10.11, 44.51, and 67.29 kcal/mol, respectively. The highest pi-pi interaction were recorded for π(C1–C3) → LP*(C5) and π(C18–C19)→ LP*(1) C21 with stabilization energy of 76.13 and 80.40 kcal/mol (Table 4).

The two N..H–C interactions can be seen from σ(N35–H35) → σ*(C6–C8) and σ(N34–H35) → σ*(C1–C3) with stabilization energy of 3.88 and 3.44 kcal/mol. The hyperconjugative interaction energy E(2) is most dominant for C-lone pair followed by pi-pi interactions between Carbons.

3.4.3. Electronic properties and global reactivity descriptors

To predict the chemical reactivity and stability of compounds, DFT global parameters are calculated [61,62]. In our current investigation, we calculated the ionization potential (IP), electron affinity (EA), chemical hardness (Ƞ), chemical potential (μ), and electronegativity (χ) to better understand the chemical reactivity and structural features of the title salt. The chemical potential (eq. iv) and the global hardness (Ƞ, eq. vi) are defined by the first- and second-order partial derivatives of total energy (E) with respect to the number of electrons (N) at constant external potential v(r), e.

$$\text{Ionization potential (IP)} = \text{- E (HOMO)} \tag{i}$$

$$\text{Electron affinity (EA)} = \text{- E (LUMO)} \tag{ii}$$

The computed ionization potential (IP, Eq. i) and electron affinity can be used to predict the electronic properties and electronic stability of the studied crystal. The IP and EA values are obtained by *Koopmans* approximations; the negative HOMO is represented by the IP, while the negative LUMO is represented by the EA (Eq. i-ii). The calculated ionization potential (IP) is 7.19 eV, while the observed electron affinity (EA) value is 1.96. The significant IP values suggest its better electronic stability where it has increased electronegativity. The significant EA value shows its strong tendency to grab valence electrons and least electropositive nature. The chemical hardness determines how resistant a cluster of nuclei and electrons is to variations in the distribution of its electrons. The determined value of chemical hardness is 2.61 eV, while the chemical potential value is −4.57 eV. The obtained smaller value of chemical hardness suggests its soft nature and reactivity toward incoming reagents. The quantitative descriptors of chemical reactivity and stability are shown by following set of equations (IV-IX) [63,64];

$$\eta = \frac{1}{2}\left(\frac{\partial^2 E}{\partial N^2}\right)\left(\frac{\partial^2 E}{\partial N^2}\right)_{V(r)} = \frac{1}{2}\left(\frac{\partial E}{\partial N}\right)_{V(r)} \tag{iii}$$

$$\text{Chemical Hardness } (\eta) = \tfrac{1}{2}\,(\text{IP- EA}) \tag{iv}$$

$$\mu = -\chi = \left(\frac{\partial E}{\partial N}\right)_{V(r)} \tag{v}$$

$$\text{Chemical potential } (\mu) = \text{-}\frac{\text{IP} + \text{EA}}{2} \tag{vi}$$

$$\text{Electronegativity } (\chi) = \text{-}\mu \tag{vii}$$

$$\text{Electrophilicity index } (\omega) = \mu^2/2\eta \tag{viii}$$

The electrophilicity index (ω, eq. viii), describes a compound's quantitative characteristics. It serves as an indicator of the amount of energy lost because of the maximum amount of electron movement between the donor and acceptor. The estimated values are useful to comprehend the toxicity of pollutants based on reactivity and site selectivity, and they also reflect the biological activity of the examined substances. The obtained value of ω is 4.14 eV, which is quite significant and indicates its electrophilic nature.

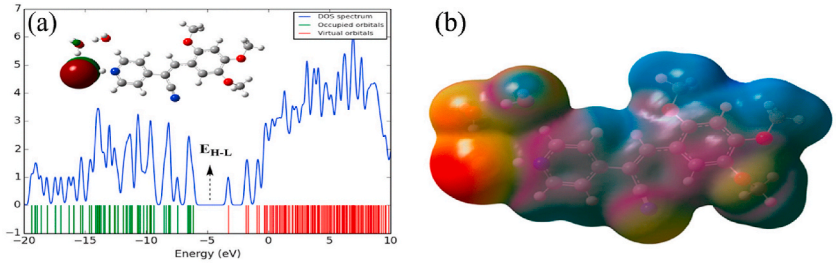

Fig. 6. a. TDOS spectrum; (b) Molecular electrostatic potential surface calculated at M06-2X/def2-TZVP.

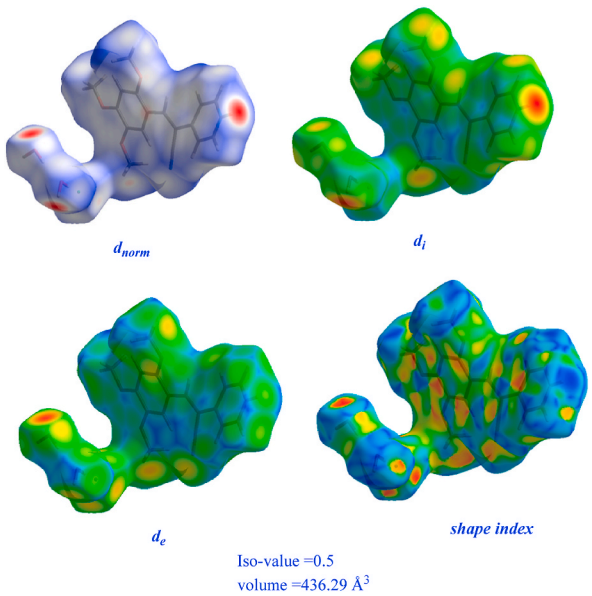

Fig. 7. Hirshfeld mapped surfaces of d_{norm}, d_i, d_e, and shape index of the studied liquid crystal.

3.4.4. DOS and MEPS analysis

To better understand the electronic and conductive characteristics of the title salt, **I**, we conducted a total density of states (TDOS) analysis using GaussSum software, and the resulting spectrum is shown in Fig. 6a. The TDOS spectrum is displayed between the energy ranges of −20 to 10 eV, with the dotted line indicating the energy of the largest filled molecular orbital (HOMO). In Fig. 6a, the green lines represent the HOMO energy, while the red lines represent the LUMO energy. The higher HOMO energies have narrowed the related $\mathbf{E_{H\text{-}L}}$ gap. As a result, the produced higher energy states of the HOMO are advantageous for enhancing the electrical properties of the title salt.

The molecular electrostatic potential (MEP) is a three-dimensional map showing how molecules are charged and other characteristics of molecules linked to charge. Furthermore, they show the electron-rich and electron-deficient parts (i.e., atom/group) and how they have shaped the molecules. The MEP is a very helpful computational tool for studying the reactivity of molecules because it shows the charge distribution of the molecule and helps identify reacting spots. For example, an incoming electrophile will be attracted to the negative regions of the molecule. In general, the MEP's most positive and negative regions are colored blue and red, respectively, and are chosen as favorite sites for nucleophilic and electrophilic assault. In title salt **I**, the electronic density is located near the chloride ion, which is involved in the charge transfer process in the solid-state (Fig. 6b).

3.4.5. Nonlinear optical (NLO) properties

In modern days, nonlinear optical (NLO)-based materials are most desired in the areas of signal processing, laser-based endoscopy, telecommunication technologies, optical storage systems, etc. In the last few decades, researchers have made significant attempts to identify and synthesize new NLO materials for the above applications. Among the new materials, the DAST or stilbazolium-based second-order nonlinear optical materials are potentially important. Their derivatives are widely used in various hi-tech products, as mentioned earlier. The present investigated salt, **I**, also belongs to the pyridinium family, and it has fascinating electronic properties. Hence, we could expect NLO properties. For this purpose, the polarizability (α_o) and static hyperpolarizability (β_o) are computed. The nonlinear optical properties are induced by the asymmetric charge distribution and electronic density *generated under the strong*

Table 6
Hirshfeld analysis of title salt, **I, C_{17} $H_{21}Cl$ N_2O_5** (in Å).

C_{17} $H_{21}Cl$ N_2O_5			
Surface parameters	Minimum	Mean	Maximum
d_i	0.7205	1.6549	2.4541
de	0.7212	1.6671	2.3459
d_{norm}	−0.5939	0.3991	1.2373
Shape index	−0.9981	0.2474	0.9978
curvedness	−4.0570	−1.0139	0.3059
Fragment patch	0.00	11.4071	35.000

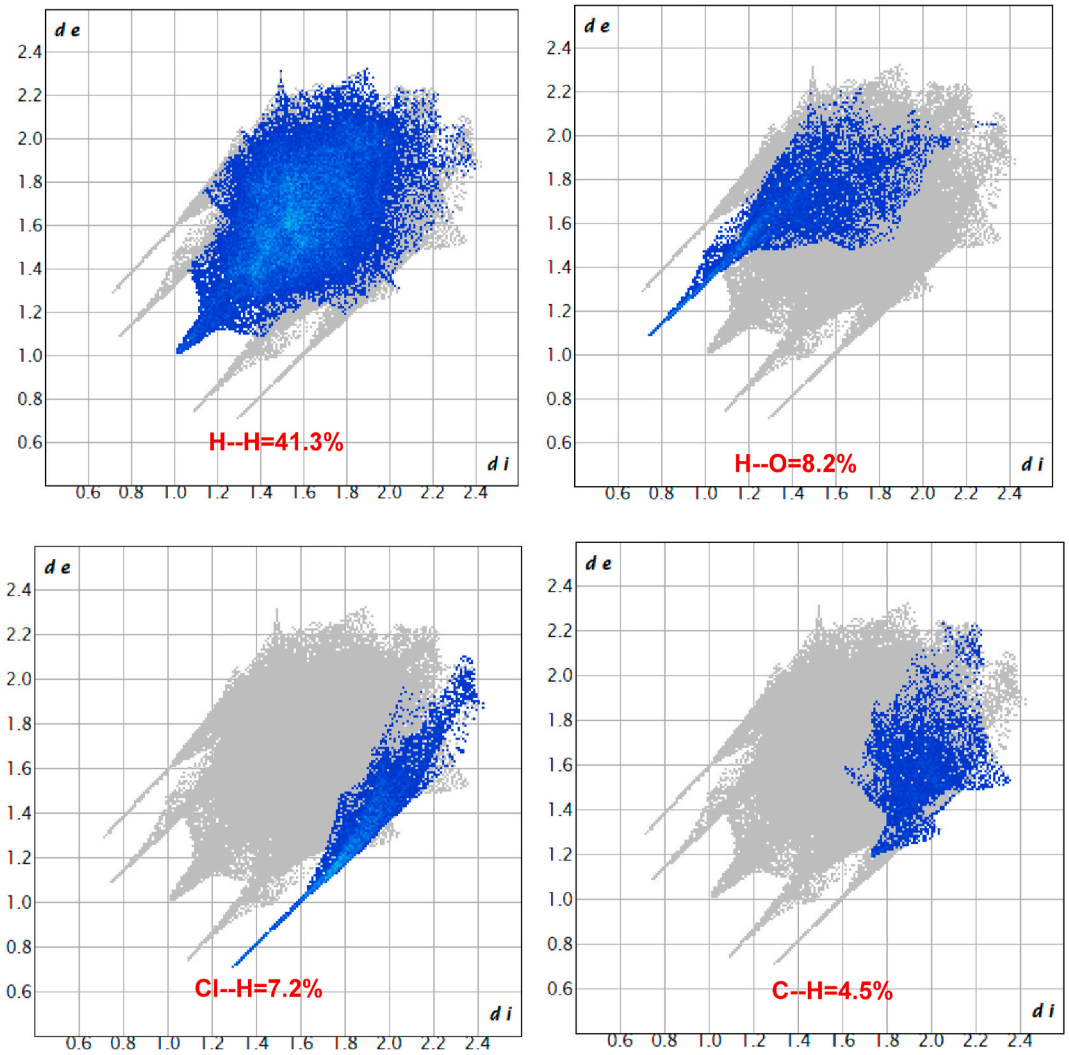

Fig. 8. Plotted d_e (external) versus *di* (internal atoms) 2D fingerprint spectra for dominant interactions.

electricity of light. The energy of the perturbed system is described by the Taylor expansion (ix).

$$E = E^O - \mu_i F_i - \left[\frac{1}{2!}\right]\alpha_{ij}F_iF_j - \frac{1}{3!}\beta_{ijk}F_iF_jF_k - \left[\frac{1}{4!}\right]\gamma_{ijkl}F_iF_jF_kF_l \quad \text{(ix)}$$

The polarizability (α_o) and static hyperpolarizability (β_o) are given by the following relation:

$$\alpha_0 = \frac{1}{3}(axx + ayy + azz) \quad \text{(x)}$$

Table 7
Intermolecular interaction energy for **I**, (Z)-4-(1-cyano-2-(2,4,5-trimethoxyphenyl) vinyl)pyridin-1-ium chloride (in kcal/mol).

N	Symmetry	R	E_{ele}	E_{pol}	E_{dis}	E_{rep}	E_{tot}
1	-x, -y, -z	4.04	−4.04	−3.25	−25.58	13.81	−18.08
1	-x, y, -z+1/2	3.75	2.51	−2.89	−27.59	15.38	−11.7
1	-x, -y, -z	9.58	−1.79	−0.98	−2.58	1.86	−3.27
2	-x, y, -z+1/2	9.87	−0.69	−0.38	−1.58	0.74	−1.79
2	x, y, z	9.13	−0.24	−0.6	−3.01	2.17	−1.6

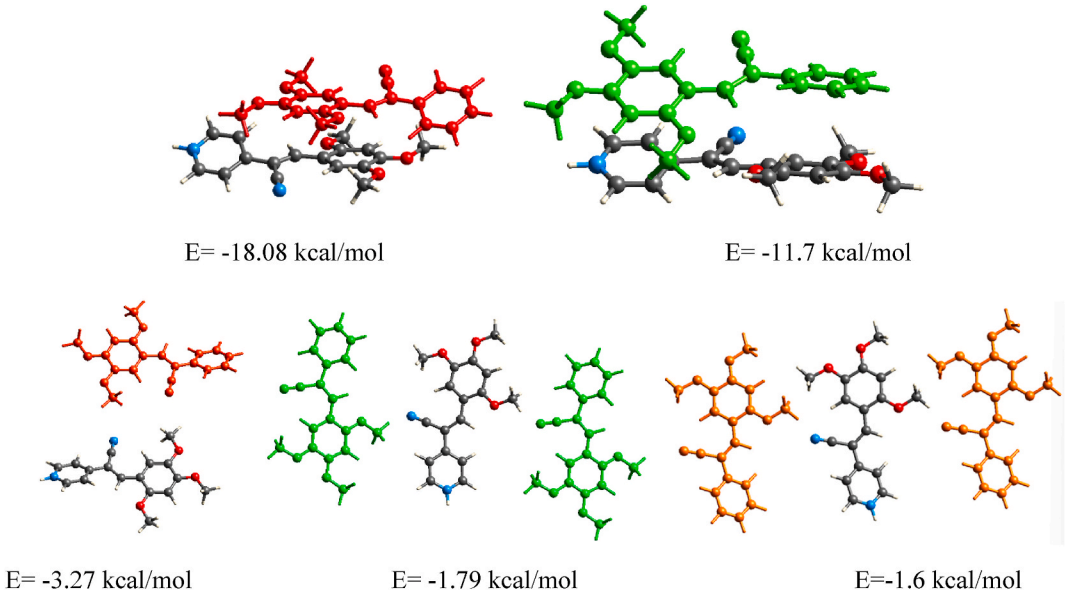

Fig. 9. Intermolecular interactions in various dimers between two cation units in **I**. (energy in kcal/mol).

$$\beta_0 = \sqrt{(\beta^2 x + (\beta^2 y + (\beta^2 z)} \quad \text{(xi)}$$

The calculated values of the linear optical response (α_o) and hyperpolarizability (β_o) are given in Table 4. The calculated α_o value is 324.297 au, while the β_o value is recorded up to 6856.34 au. The obtained noticeable value of α_o shows its linear optical properties and extent of asymmetrical charge distribution in the structure. The α_o value further shows the polarizable nature of the molecule and its interesting features for designing modern optoelectronic materials. The estimated value of β_o also increased to 6856.34 au, indicating a nonlinear response to externally induced electric fields. Based on these results, we conclude that the title salt, **I**, has significant potential for NLO and interesting optoelectrical properties.

3.4.6. Hirshfeld surface (HS) analysis

The HS analysis associated with two-dimensional fingerprint plots was generated using Crystal Explorer 17.5. HS analysis effectively examines the X-ray data and visualizes intermolecular interactions in the crystalline state [65,66]. The potential short intermolecular contacts (less than the sum of vdW radii of interacting atoms) show red spots on the HS (Fig. 7). The HS of the studied liquid crystal $C_{17}H_{21}ClN_2O_5$ mapped over d_{norm}, d_i, d_e, and *shape index* are given in Fig. 7. In the plotted d_{norm}, the presence of red color near the water molecules indicates its reactive site to neighbor molecules. The HS parameters for the $C_{17}H_{21}ClN_2O_5$ crystal are given in Table 6. The d_{norm} value ranges from −0.5939 to a maximum of 1.2373 Å. The maximum value for fragment patches increased to 35.00 Å, while d_e increased to 2.3459 Å.

The plotted 2D fingerprint images provide information about the type of intermolecular contact between atoms and their crucial interactions. These interactions are plotted between d_e (external) versus *di* (internal atoms). The plotted spectra for dominant interactions inside to outside are given in Fig. 8. In the crystal, the highest inside-to-outside is found for H···H (41.3 %), followed by H···O interactions up to 8.1 %. Similarly, the Cl···H interaction is 7.2 %, while the lowest interaction of the central fragment with the neighbor is 4.5 %, which is calculated for carbon and hydrogen (C···H).

3.4.7. Non-covalent interaction (NCI) index analysis

To understand the nature of the non-covalent interaction topology between a cation, anion (Cl^-) and H_2O, molecules were used to generate energy frameworks for **I** and the precursor, as mentioned in the experimental section. Different molecular dimers were

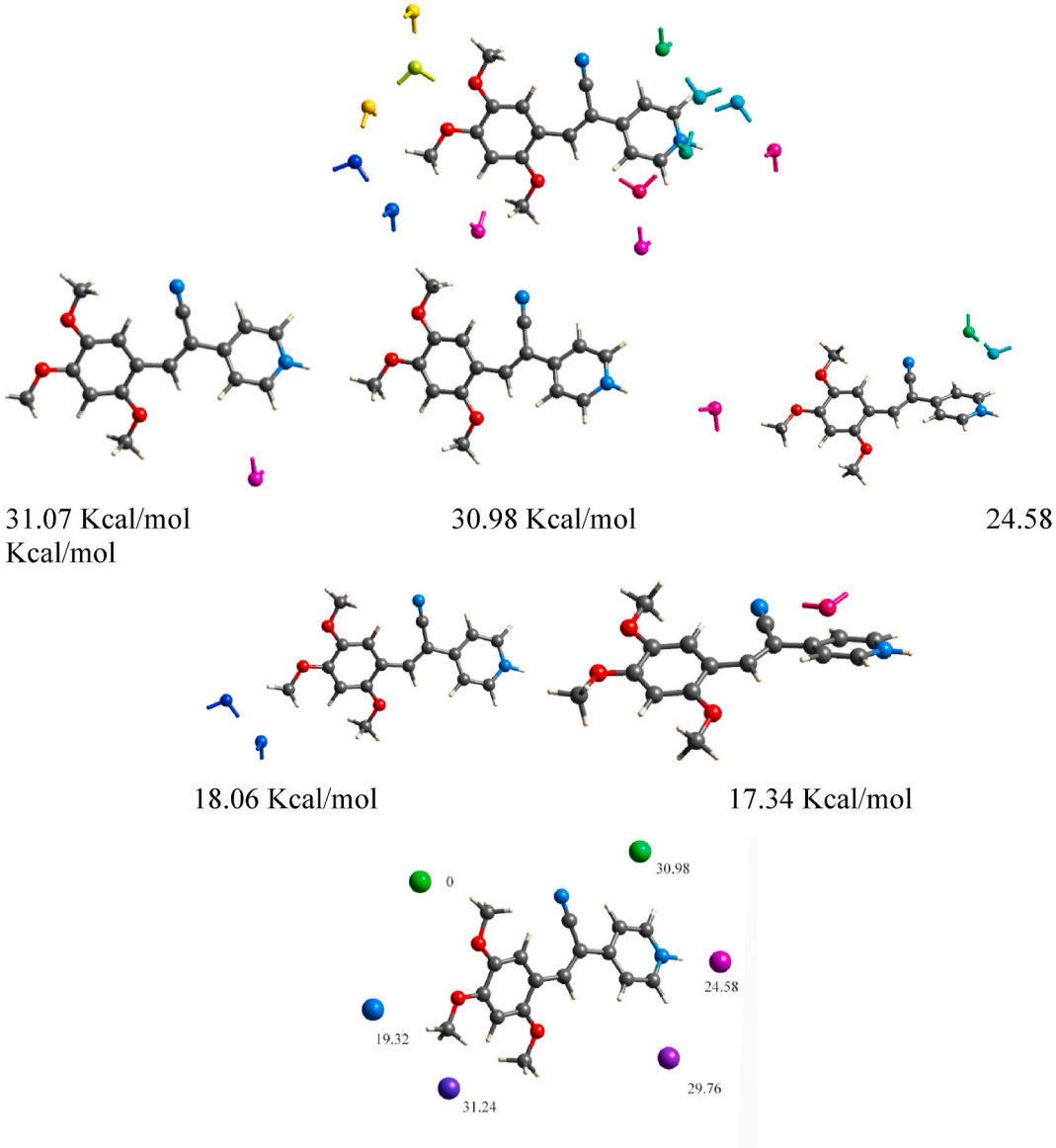

Fig. 10. Intermolecular interactions in various dimers between cation, anion and water molecules in the **I**. (energy in kcal/mol).

extracted from the Crystalexplorer [67] energy analysis, and topological analysis was performed using the AIMALL program [50]. For this, the wave functions were generated from the energy calculation of the obtained dimers (the geometry of the crystalline structure with the normalized H that involves distances to their typical neutron values) at theory level M06-2X-D3/cc-pVTZ [68]. The intermolecular interactions present in the crystal packing of **I** were quantified by separating electrostatic, dispersion, polarization and repulsion forces, as shown in Table 7. The interaction between two molecules of **I**, Fig. 9, showed that the total energies of −18.08 and −11.70 kcal/mol were greater than that of the precursor (OPUSEA) that interacts with two molecules in Fig. S4 and Table S6.

The dispersion contribution predominantly stabilizes all the dimers in the title salt. The antiparallel π stacking interaction in the dimer helps to arrange the molecules in the column manor in salt **I**, whereas the parallel π stacking interaction in precursor molecules (OPUSEA) favors arranging in the typical herringbone architecture (Fig. S4). Additionally, pyridinium nitrogen, chloride ions, and water molecules are involved in the various intermolecular interactions and are significantly involved in stabilizing crystal packing (Fig. 10, Figs. S5 and S6, and Tables S7 and S8).

3.4.8. QTAIM topological features of intermolecular interactions

The topology of the calculated electron density at the M06-2X-D3/cc-pVTZ level of theory was analyzed using Bader's quantum theory of atoms in molecules (QTAIM) approach. According to QTAIM, a chemical bond is distinctively described by a line of maximum electron density linking two bonded atoms (bond path, BP) on which a critical bond point (3, 1) is present (BCP) [69,70].

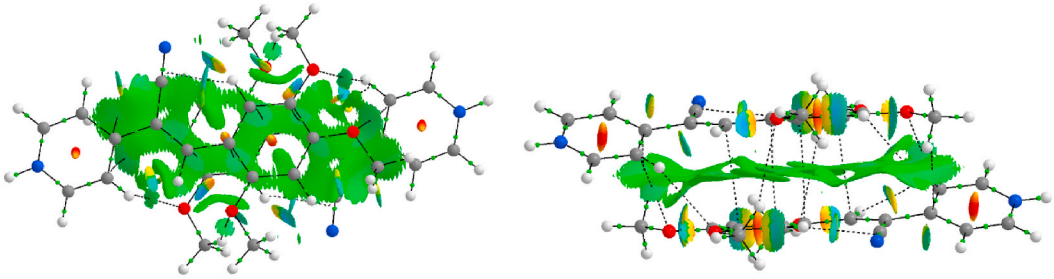

Dimer 1

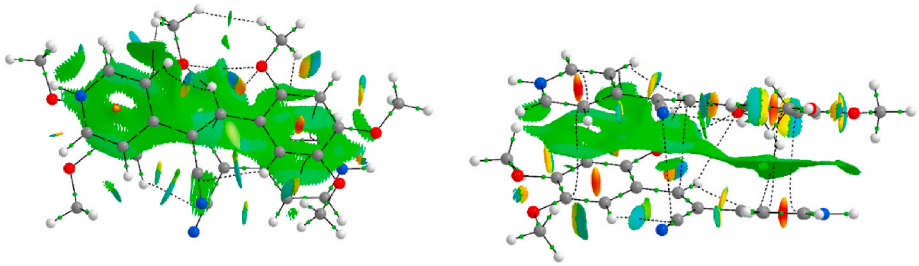

Dimer 2

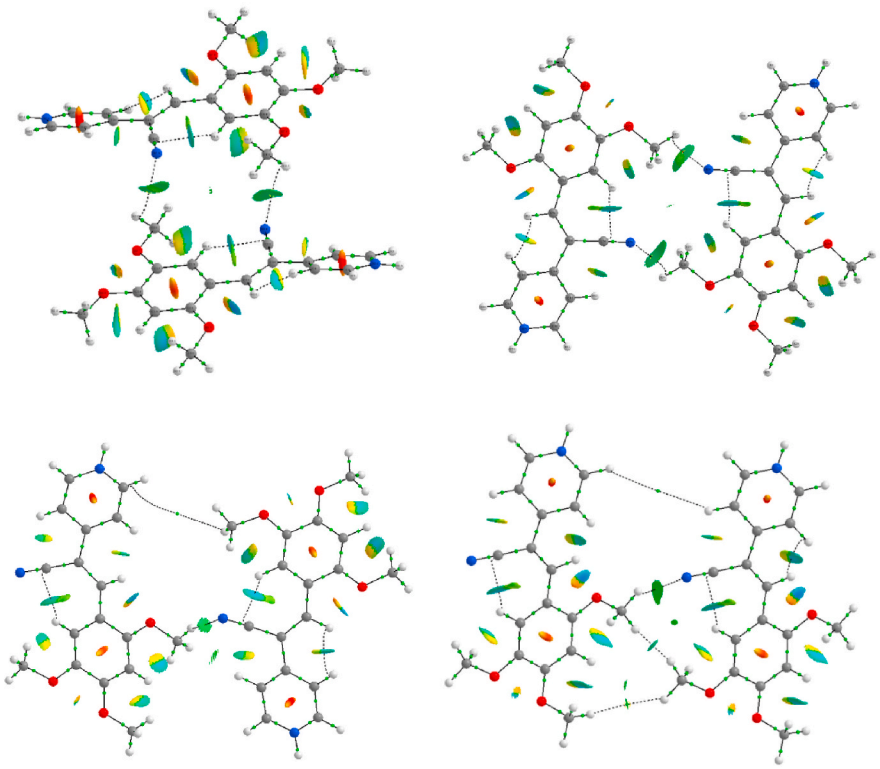

Fig. 11. Molecular graphs showing intra- and intermolecular interactions in **I** and non-covalent interactions (NCI). A green extended isosurface can be observed between the two dimers due to π–π interactions.

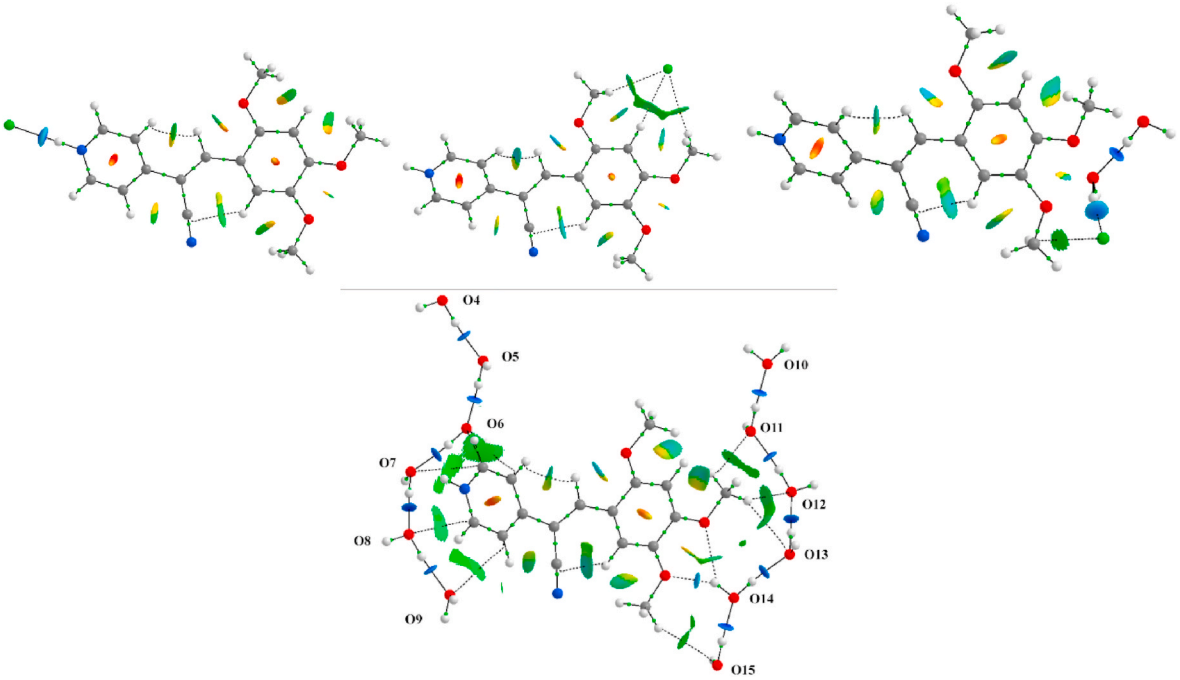

Fig. 12. Formation of molecular sheets associated with NCI intermolecular interactions of **I** with Cl^{-} and molecules of H_2O.

The analysis was performed using the AIMALL program [50]. Koch and Popelier [71] quantified that a hydrogen bond would be present in the molecular topology if the electron density is within the range of 0.002–0.040 atomic units (a.u.) and the resultant Laplacian within the range of 0.024–0.139 a.u [40,54]. results (BCP), electron density ρ(r) in the BCP, Laplacian of the electron density $\nabla^2\rho(r)$, and the interaction of H and the acceptor atom were obtained, and the bonding (r_D and r_D) and nonbonding radii of the donor (r_D^0) and acceptor (r_D^0) atoms were compared. The fourth criterion of KP(KP-4) describes the mutual penetration of the H atom and the acceptor atom and differentiates the H-bonding character from the van der Waals type. For a typical hydrogen bond, the values of $\Delta{=}(r_D^o - r_D) > \Delta{=}(r_A^o - r_A)$ and $\Delta r_D + \Delta r_A > 0$ represent positive interpenetration. If either or both conditions are violated, then the interaction is said to be Waals in nature [70,72]. The hydrogen-bond interactions may be categorized as follows: strong and covalent hydrogen bond $\nabla^2\rho(r) < 0$ and $H < 0$; medium and partially covalent hydrogen bond, $\nabla^2\rho(r) > 0$ and $H < 0$; and weak and electrostatic hydrogen bond, when $\nabla^2\rho(r) > 0$ and $H > 0$ [12,13].

It is observed in Fig. 11 that the BCP with NCI isosurfaces indicated that the π····π stacking interactions are distributed throughout the molecule, unlike the precursor (OPUSEA), Table S9 and Fig. S7. The values (Table S10) indicated that the interactions that dominate the crystal packing are van der Waals interactions in **I** and OPUSEA. The differences are in the hydrogen bonds, Fig. 12 and Tables S10 and S11. For **I**, two successive molecular dimer sheets associated with NH···Cl, bifurcated C–H····Cl interactions, and OW–H····Cl are present; the first is a medium and partially covalent hydrogen bond, and the others are strong and covalent hydrogen bonds. Therefore, the participation of the Cl anion and H_2O changes the crystal packing, as well as the interactions [37,73]. The results allow us to evaluate that the interactions increase the aggregation of molecules and therefore influence the color of the molecules.

4. Conclusion

The changes in color, optical absorption, and charge transfer of (Z)-4-(1-cyano-2-(2,4,5-trimethoxyphenyl)vinyl) pyridin-1-ium chloride were analyzed by several experimental and computational techniques. The results evidenced the interaction, at the molecular level, of organic compounds with acid to form a salt along with the importance of non-covalent interactions. These interactions along with packing lead to structural modifications such as changes in structural torsion and bond length, especially in the pyridinium ring when compared with the precursor compound. The structural changes favored intermolecular interactions, as well as charge transfer, which is enhanced in the pyridinium salt by hydrogen bonds and non-covalent interactions. The charge distribution in the molecule was also affected, leading to a lower HOMO-LUMO energy gap; in this case, both HOMO and LUMO values were modified. The intermolecular interactions were also affected by the presence of Cl anions and H_2O molecules in the crystal structure of the pyridinium salt. All these features are the reason for changes in physical properties such as color, dipole moment, and nonlinear optics.

Funding statement

The authors would like to thank VIEP-BUAP ([grant 00110-VIEP-2022) and CONAHCYT CF-2019-51472 for financial support.

Data availability statement

Data associated with this study has been deposited at the Cambridge Crystallographic Data Centre (www.ccdc.cam.ac.uk/data_request/cif) under the accession number CCDC-2257300.

CRediT authorship contribution statement

Enrique Pérez-Gutiérrez: Funding acquisition, Writing – review & editing, Conceptualization, Investigation. **Atazaz Ahsin:** Data curation, Formal analysis, Investigation. **Youness El Bakri:** Conceptualization, Formal analysis, Methodology, Writing – original draft. **Perumal Venkatesan:** Data curation, Methodology. **S. Thamotharan:** Data curation, Formal analysis, Software, Writing – review & editing. **M. Judith Percino:** Conceptualization, Funding acquisition, Methodology, Software, Validation, Writing – original draft.

Declaration of competing interest

The authors declare that they have no known competing financial interests or personal relationships that could have appeared to influence the work reported in this paper.

Acknowledgements

Authors hanks to Laboratorio Nacional de Supercómputo del Sureste (LNS-BUAP) for computational resources and Catedras CONACYT.

Appendix A. Supplementary data

Supplementary data to this article can be found online at https://doi.org/10.1016/j.heliyon.2023.e21040.

References

[1] M. Gordel-Wójcik, M. Nyk, A. Bajorek, E. Zych, M. Samoć, B. Jędrzejewska, Synthesis and optical properties of linear and branched styrylpyridinium dyes in different environments, J. Mol. Liq. 356 (2022), 119007, https://doi.org/10.1016/j.molliq.2022.119007.
[2] M.D. Milošević, N.Ž. Prlainović, M. Milčić, V. Nikolić, A. Božić, M. Bigović, A.D. Marinković, Solvent, structural, quantum chemical study and antioxidative activity of symmetrical 1-methyl-2,6-bis[2-(substituted phenyl)ethenyl]pyridinium iodides, J. Iran. Chem. Soc. 15 (2018) 2483–2501, https://doi.org/10.1007/s13738-018-1437-5.
[3] C. Pigot, G. Noirbent, T.-T. Bui, S. Péralta, S. Duval, D. Gigmes, M. Nechab, F. Dumur, Synthesis, and the optical and electrochemical properties of a series of push–pull dyes based on the 4-(9-ethyl-9 *H* -carbazol-3-yl)-4-phenylbuta-1,3-dienyl donor, New J. Chem. 45 (2021) 5808–5821, https://doi.org/10.1039/D1NJ00275A.
[4] A. Shimizu, Y. Ishizaki, S. Horiuchi, T. Hirose, K. Matsuda, H. Sato, J. Yoshida, HOMO–LUMO energy-gap tuning of π-conjugated Zwitterions Composed of electron-donating anion and electron-accepting cation, J. Org. Chem. 86 (2021) 770–781, https://doi.org/10.1021/acs.joc.0c02343.
[5] S. Ellinger, K.R. Graham, P. Shi, R.T. Farley, T.T. Steckler, R.N. Brookins, P. Taranekar, J. Mei, L.A. Padilha, T.R. Ensley, H. Hu, S. Webster, D.J. Hagan, E.W. Van Stryland, K.S. Schanze, J.R. Reynolds, Donor–Acceptor–Donor-based π-conjugated Oligomers for nonlinear optics and near-IR emission, Chem. Mater. 23 (2011) 3805–3817, https://doi.org/10.1021/cm201424a.
[6] P. Bosch, F. Catalina, T. Corrales, C. Peinado, Fluorescent probes for sensing processes in Polymers, Chem. Eur J. 11 (2005) 4314–4325, https://doi.org/10.1002/chem.200401349.
[7] K. Nivetha, W. Madhuri, Structural, spectral, thermal, and optical studies of stilbazolium derivative crystal: (E)-4-(3-hydroxy-4-methoxystyryl)-1-methyl pyridinium iodide monohydrate, Opt Laser. Technol. 109 (2019) 496–503, https://doi.org/10.1016/j.optlastec.2018.08.035.
[8] K. Anandhan, M. Cerón, P. Ceballos, R. Ramos-Hernández, V. Perumal, E. Pérez-Gutiérrez, M. Sosa-Rivadeneyra, S. Thamotharan, M.J. Percino, ^{1}H-NMR, photophysical, and pH studies of 4-(4,5-Diphenyl-1H-imidazole-2-yl)benzaldehyde through experimental and DFT theoretical analysis, ChemistrySelect 5 (2020), https://doi.org/10.1002/slct.201904505.
[9] S. Kansız, A. Tolan, M. Azam, N. Dege, M. Alam, Y. Sert, S.I. Al-Resayes, H. İçbudak, Acesulfame based Co(II) complex: synthesis, structural investigations, solvatochromism, Hirshfeld surface analysis and molecular docking studies, Polyhedron 218 (2022), 115762, https://doi.org/10.1016/j.poly.2022.115762.
[10] J.L.R. Williams, S.K. Webster, J.A. Van Allan, Cis and trans Isomers of 2-Styrylpyridine, J. Org. Chem. 26 (1961) 4893–4895, https://doi.org/10.1021/jo01070a027.
[11] K. Takagi, B.R. Suddaby, S.L. Vadas, C.A. Backer, Photochemical reactions in organized assemblies. 49. Topological control of reactivity by interfacial orientation: excimer fluorescence and photodimerization of 4-stilbazolium cations in aerosol Ot reversed micelles, J. Am. Chem. Soc. 108 (1986) 7865–7867, https://doi.org/10.1021/ja00284a079.
[12] H. Shayira Banu, A. Lalitha, C. Srinivasan, K. Pitchumani, Modification of photochemical reactivity of trans-2-styrylpyridine: effect of cyclodextrin complexation, Chem. Commun. (1999) 607–608, https://doi.org/10.1039/a809372e.
[13] Z. Yang, S. Aravazhi, A. Schneider, P. Seiler, M. Jazbinsek, P. Günter, Synthesis and crystal growth of stilbazolium derivatives for second-order nonlinear optics, Adv. Funct. Mater. 15 (2005) 1072–1076, https://doi.org/10.1002/adfm.200500036.
[14] S. Kannan, A. Sekar, K. Sivaperuman, Effects of the molecular structure on the second-order nonlinear optical properties of stilbazolium derivative single crystals: a review, J. Mater. Chem. C 8 (2020) 16668–16690, https://doi.org/10.1039/D0TC04260A.
[15] A. Bajorek, K. Trzebiatowska, B. Jędrzejewska, M. Pietrzak, R. Gawinecki, J. Pączkowski, Developing of fluorescence probes based on stilbazolium salts for monitoring free radical polymerization processes. II, J. Fluoresc. 14 (2004) 295–307, https://doi.org/10.1023/B:JOFL.0000024562.60225.d0.
[16] S. Wróblewski, K. Trzebiatowska, B. Jędrzejewska, M. Pietrzak, R. Gawinecki, J. Pączkowski, Development of fluorescence probes based on stilbazolium salts for monitoring free radical polymerization processes, J. Chem. Soc. Perkin Trans. 2 (1999) 1909–1917, https://doi.org/10.1039/a902904d.
[17] B. Strehmel, Photophysical properties of fluorescence probes I: dialkylamino stilbazolium dyes, J. Biomed. Opt. 1 (1996) 98, https://doi.org/10.1117/12.227538.

[18] S.R. Marder, J.W. Perry, Molecular materials for second-order nonlinear optical applications, Adv. Mater. 5 (1993) 804–815, https://doi.org/10.1002/adma.19930051104.

[19] X. Liu, Z. Yang, D. Wang, H. Cao, Molecular structures and second-order nonlinear optical properties of ionic organic crystal materials, Crystals 6 (2016) 158, https://doi.org/10.3390/cryst6120158.

[20] S. Sohma, H. Takahashi, T. Taniuchi, H. Ito, Organic nonlinear optical crystal DAST growth and its device applications, Chem. Phys. 245 (1999) 359–364, https://doi.org/10.1016/S0301-0104(99)00060-9.

[21] B. Ruiz, Z. Yang, V. Gramlich, M. Jazbinsek, P. Günter, Synthesis and crystal structure of a new stilbazolium salt with large second-order optical nonlinearity, J. Mater. Chem. 16 (2006) 2839–2842, https://doi.org/10.1039/B603049A.

[22] J. Yin, L. Li, Z. Yang, M. Jazbinsek, X. Tao, P. Günter, H. Yang, A new stilbazolium salt with perfectly aligned chromophores for second-order nonlinear optics: 4-N,N-Dimethylamino-4′-N′-methyl-stilbazolium 3-carboxy-4-hydroxybenzenesulfonate, Dye. Pigment. 94 (2012) 120–126, https://doi.org/10.1016/j.dyepig.2011.12.004.

[23] B. Jędrzejewska, J. Kabatc, M. Pietrzak, J. Pączkowski, Hemicyanine dyes: synthesis, structure and photophysical properties, Dye, Pigment 58 (2003) 47–58, https://doi.org/10.1016/S0143-7208(03)00035-4.

[24] S. Trupp, A. Schweitzer, G.J. Mohr, Fluororeactands for the detection of Saccharides based on hemicyanine dyes with a Boronic acid Receptor, Microchim. Acta 153 (2006) 127–131, https://doi.org/10.1007/s00604-005-0470-0.

[25] O. Simsek, M. Ashfaq, M.N. Tahir, S. Ozturk, E. Agar, Synthesis and Charaterizations of the Schiff base derived from 2-hydroxy-5-Nitrobenzaldehyde Alongwith Hirshfeld surface analysis and computational study, J. Struct. Chem. 64 (2023) 942–953, https://doi.org/10.1134/S0022476623050128.

[26] I. Kikaš, B. Carlotti, I. Škorić, M. Šindler-Kulyk, U. Mazzucato, A. Spalletti, Synthesis, spectral properties and photobehaviour of push–pull distyrylbenzene nitro-derivatives, J. Photochem. Photobiol. Chem. 244 (2012) 38–46, https://doi.org/10.1016/j.jphotochem.2012.06.009.

[27] M. Sowmiya, A.K. Tiwari, Sonu, S.K. Saha, Study on intramolecular charge transfer fluorescence properties of trans-4-[4′-(N,N′-dimethylamino)styryl]pyridine: effect of solvent and pH, J. Photochem. Photobiol. Chem. 218 (2011) 76–86, https://doi.org/10.1016/j.jphotochem.2010.12.006.

[28] B. Jędrzejewska, M. Pietrzak, J. Pączkowski, Solvent effects on the spectroscopic properties of Styrylquinolinium dyes series, J. Fluoresc. 20 (2010) 73–86, https://doi.org/10.1007/s10895-009-0524-5.

[29] L. Mencaroni, A. Cesaretti, F. Elisei, I. Škorić, M. Mlakić, A. Spalletti, Acid–base strength and acido(fluoro)chromism of three push–pull derivatives of 2,6-distyrylpyridine, Photochem. Photobiol. Sci. 21 (2022) 935–947, https://doi.org/10.1007/s43630-022-00184-5.

[30] M. Todorova, R. Bakalska, T. Kolev, Synthesis, crystal structure, and spectroscopic properties of new stilbazolium salt with enlarged π-conjugated system, Spectrochim. Acta Part A Mol. Biomol. Spectrosc. 108 (2013) 211–222, https://doi.org/10.1016/j.saa.2013.01.088.

[31] M. Vendrell, D. Zhai, J.C. Er, Y.-T. Chang, Combinatorial Strategies in fluorescent probe Development, Chem. Rev. 112 (2012) 4391–4420, https://doi.org/10.1021/cr200355j.

[32] Q. Wu, J. Liu, Y. Li, M.M.S. Lee, L. Hu, Y. Li, P. Zhou, D. Wang, B.Z. Tang, Janus luminogens with bended intramolecular charge transfer: toward molecular transistor and brain imaging, Matter 4 (2021) 3286–3300, https://doi.org/10.1016/j.matt.2021.08.002.

[33] L. Fan, Y.-J. Fu, Q.-L. Liu, D.-T. Lu, C. Dong, S.-M. Shuang, Novel far-visible and near-infrared pH probes based on styrylcyanine for imaging intracellular pH in live cells, Chem, Commun. Now. 48 (2012), 11202, https://doi.org/10.1039/c2cc35363f.

[34] M. Panigrahi, S. Dash, S. Patel, B.K. Mishra, Syntheses of cyanines: a review, Tetrahedron 68 (2012) 781–805, https://doi.org/10.1016/j.tet.2011.10.069.

[35] T. Deligeorgiev, A. Vasilev, S. Kaloyanova, J.J. Vaquero, Styryl dyes – synthesis and applications during the last 15 years, Color, Technol. 126 (2010) 55–80, https://doi.org/10.1111/j.1478-4408.2010.00235.x.

[36] V. Palakollu, S. Kanvah, α-Cyanostilbene based fluorophores: aggregation-induced enhanced emission, solvatochromism and the pH effect, New J. Chem. 38 (2014) 5736–5746, https://doi.org/10.1039/C4NJ01103A.

[37] P. Venkatesan, M. Cerón, E. Pérez-Gutiérrez, A.E. Castillo, S. Thamotharan, F. Robles, M.A. Siegler, M.J. Percino, Experimental and theoretical insights into the optical properties and intermolecular interactions in push-pull bromide salts, ChemistryOpen 8 (2019) 483–496, https://doi.org/10.1002/open.201900061.

[38] I. Iribarren, G. Sánchez-Sanz, I. Alkorta, J. Elguero, C. Trujillo, Evaluation of electron density shifts in noncovalent interactions, J. Phys. Chem. A. 125 (2021) 4741–4749, https://doi.org/10.1021/acs.jpca.1c00830.

[39] A.A. El-Emam, E. Saveeth Kumar, K. Janani, L.H. Al-Wahaibi, O. Blacque, M.I. El-Awady, N.H. Al-Shaalan, M.J. Percino, S. Thamotharan, Quantitative assessment of the nature of noncovalent interactions in *N* -substituted-5-(adamantan-1-yl)-1,3,4-thiadiazole-2-amines: insights from crystallographic and QTAIM analysis, RSC Adv. 10 (2020) 9840–9853, https://doi.org/10.1039/D0RA00733A.

[40] I. Alkorta, J. Elguero, A. Frontera, Not only hydrogen bonds: other noncovalent interactions, Crystals 10 (2020) 180, https://doi.org/10.3390/cryst10030180.

[41] S. Thamotharan, J. Kothandapani, S. Selva Ganesan, N.S. Venkataramanan, S. Madan Kumar, K. Byrappa, J. Percino, F. Robles, Quantitative analysis of intermolecular interactions in 2,2'-((4-bromophenyl)methylene)bis(3-hydroxy-5,5-dimethylcyclohex-2-en-1-one): insights from crystal structure, PIXEL, Hirshfeld surfaces and QTAIM analysis, J. Chem. Sci. 130 (2018) 20, https://doi.org/10.1007/s12039-018-1421-8.

[42] R.C. Clark, J.S. Reid, The analytical calculation of absorption in multifaceted crystals, Acta Crystallogr. Sect. A Found. Crystallogr. 51 (1995) 887–897, https://doi.org/10.1107/S0108767395007367.

[43] G.M. Sheldrick, *Shelxt* – Integrated space-group and crystal-structure determination, Acta Crystallogr. Sect. A Found. Adv. 71 (2015) 3–8, https://doi.org/10.1107/S2053273314026370.

[44] M.J. Frisch, G.W. Trucks, H.B. Schlegel, G.E. Scuseria, M.A. Robb, J.R. Cheeseman, G. Scalmani, V. Barone, G.A. Petersson, H. Nakatsuji, X. Li, M. Caricato, A. V. Marenich, J. Bloino, B.G. Janesko, R. Gomperts, B. Mennucci, H.P. Hratchian, J.V. Ortiz, A.F. Izmaylov, J.L. Sonnenberg, D. Williams-Young, F. Ding, F. Lipparini, F. Egidi, J. Goings, B. Peng, A. Petrone, T. Henderson, D. Ranasinghe, V.G. Zakrzewski, J. Gao, N. Rega, G. Zheng, W. Liang, M. Hada, M. Ehara, K. Toyota, R. Fukuda, J. Hasegawa, M. Ishida, T. Nakajima, Y. Honda, O. Kitao, H. Nakai, T. Vreven, K. Throssell, J.A. Montgomery Jr., J.E. Peralta, F. Ogliaro, M.J. Bearpark, J.J. Heyd, E.N. Brothers, K.N. Kudin, V.N. Staroverov, T.A. Keith, R. Kobayashi, J. Normand, K. Raghavachari, A.P. Rendell, J.C. Burant, S. S. Iyengar, J. Tomasi, M. Cossi, J.M. Millam, M. Klene, C. Adamo, R. Cammi, J.W. Ochterski, R.L. Martin, K. Morokuma, O. Farkas, J.B. Foresman, D.J. Fox, Gaussian 09, Revision C.01, Gaussian, Inc., Wallingford CT, 2009.

[45] A.D. Becke, Density-functional thermochemistry. III. The role of exact exchange, J. Chem. Phys. 98 (1993) 5648–5652, https://doi.org/10.1063/1.464913.

[46] C. Lee, W. Yang, R.G. Parr, Development of the Colle-Salvetti correlation-energy formula into a functional of the electron density, Phys. Rev. B 37 (1988) 785–789, https://doi.org/10.1103/PhysRevB.37.785.

[47] B. Miehlich, A. Savin, H. Stoll, H. Preuss, Results obtained with the correlation energy density functionals of becke and Lee, Yang and Parr, Chem. Phys. Lett. 157 (1989) 200–206, https://doi.org/10.1016/0009-2614(89)87234-3.

[48] M.A. Spackman, D. Jayatilaka, Hirshfeld surface analysis, CrystEngComm 11 (2009) 19–32, https://doi.org/10.1039/B818330A.

[49] J.J. McKinnon, M.A. Spackman, A.S. Mitchell, Novel tools for visualizing and exploring intermolecular interactions in molecular crystals, Acta Crystallogr. Sect. B Struct. Sci. 60 (2004) 627–668, https://doi.org/10.1107/S0108768104020300.

[50] A.K. Todd, AIMALL Version 19.02.13, TK Gristmill Software, 2019.

[51] A. Bondi, van der Waals volumes and radii, J. Phys. Chem. 68 (1964) 441–451, https://doi.org/10.1021/j100785a001.

[52] A. Castillo, P. Ceballos, P. Santos, M. Cerón, P. Venkatesan, E. Pérez-Gutiérrez, M. Sosa-Rivadeneyra, S. Thamotharan, M.A. Siegler, M.J. Percino, Solution and solid-state photophysical properties of positional Isomeric acrylonitrile derivatives with Core pyridine and phenyl moieties: experimental and DFT studies, Molecules 26 (2021) 1500, https://doi.org/10.3390/molecules26061500.

[53] A. Lobato, M.A. Salvadó, J.M. Recio, M. Taravillo, V.G. Baonza, Highs and Lows of bond lengths: is there Any Limit? Angew. Chemie Int. Ed. 60 (2021) 17028–17036, https://doi.org/10.1002/anie.202102967.

[54] Usman, Jaafar Khan, Tabassum Alsalme, Structure of Imidazolium-N-phthalolylglycinate salt hydrate: combined experimental and quantum chemical calculations studies, Crystals 10 (2020) 91, https://doi.org/10.3390/cryst10020091.

[55] F.H. Allen, O. Kennard, D.G. Watson, L. Brammer, A.G. Orpen, R. Taylor, Tables of bond lengths determined by X-ray and neutron diffraction. Part 1. Bond lengths in organic compounds, J. Chem. Soc. Perkin Trans. 2 (1987) S1, https://doi.org/10.1039/p298700000s1.

[56] A. Jeffrey George, An Introduction to Hydrogen Bonding, Oxford University Press, 1997.
[57] T. Steiner, The hydrogen bond in the solid state, Angew. Chemie Int. Ed. 41 (2002) 48–76, https://doi.org/10.1002/1521-3773(20020104)41:1<48::AID-ANIE48>3.0.CO;2. U.
[58] K. Molčanov, I. Sabljić, B. Kojić-Prodić, Face-to-face π-stacking in the multicomponent crystals of chloranilic acid, alkali hydrogenchloranilates, and water, CrystEngComm 13 (2011) 4211, https://doi.org/10.1039/c1ce05161j.
[59] R. Ilmi, S. Kansız, N.K. Al-Rasbi, N. Dege, P.R. Raithby, M.S. Khan, Towards white light emission from a hybrid thin film of a self-assembled ternary samarium (<scp>iii</scp>) complex, New J. Chem. 44 (2020) 5673–5683, https://doi.org/10.1039/C9NJ06287D.
[60] P. Sen, G.Y. Atmaca, A. Erdogmus, S.D. Kanmazalp, N. Dege, S.Z. Yildiz, Peripherally tetra-benzimidazole units-substituted zinc(II) phthalocyanines: synthesis, characterization and investigation of photophysical and photochemical properties, J. Lumin. 194 (2018) 123–130, https://doi.org/10.1016/j.jlumin.2017.10.022.
[61] Mercury 3.5.1 (n.d.), http://www.ccdc.cam.ac.uk/mercury/. (Accessed 13 December 2023).
[62] O.V. Dolomanov, L.J. Bourhis, R.J. Gildea, J.A.K. Howard, H. Puschmann, *OLEX2* : a complete structure solution, refinement and analysis program, J. Appl. Crystallogr. 42 (2009) 339–341, https://doi.org/10.1107/S0021889808042726.
[63] S. Pal, N. Vaval, R. Roy, Principle of maximum hardness: an accurate ab initio study, J. Phys. Chem. 97 (1993) 4404–4406, https://doi.org/10.1021/j100119a025.
[64] L. Wang, J. Ding, L. Pan, D. Cao, H. Jiang, X. Ding, Quantum chemical descriptors in quantitative structure–activity relationship models and their applications, Chemom. Intell. Lab. Syst. 217 (2021), 104384, https://doi.org/10.1016/j.chemolab.2021.104384.
[65] O. Simsek, M. Dincer, N. Dege, E. Saif, I. Yilmaz, A. Cukurovali, Crystal structure and Hirshfeld surface analysis of (Z)-4-{[4-(3-methyl-3-phenylcyclobutyl) thiazol-2-yl]amino}-4-oxobut-2-enoic acid, Acta Crystallogr. Sect. E Crystallogr. Commun. 78 (2022) 120–124, https://doi.org/10.1107/S2056989022000032.
[66] A. Ramalingam, S. Kansız, N. Dege, S. Sambandam, Synthesis, crystal structure, DFT calculations and Hirshfeld surface analysis of 3-Chloro-2,6-bis(4-Chlorophenyl)-3-Methylpiperidin-4-one, J. Chem. Crystallogr. 51 (2021) 273–287, https://doi.org/10.1007/s10870-020-00852-3.
[67] P.R. Spackman, M.J. Turner, J.J. McKinnon, S.K. Wolff, D.J. Grimwood, D. Jayatilaka, M.A. Spackman, *CrystalExplorer* : a program for Hirshfeld surface analysis, visualization and quantitative analysis of molecular crystals, J. Appl. Crystallogr. 54 (2021) 1006–1011, https://doi.org/10.1107/S1600576721002910.
[68] S. Grimme, J. Antony, S. Ehrlich, H. Krieg, A consistent and accurate *ab initio* parametrization of density functional dispersion correction (DFT-D) for the 94 elements H-Pu, J. Chem. Phys. 132 (2010), 154104, https://doi.org/10.1063/1.3382344.
[69] R.F.W. Bader, Atoms in Molecules A Quantum Theory, A Clarendon Press Publication International Series of Monographs on Chemistry, Oxford University Press, Oxford, UK, 1994.
[70] R.F.W. Bader, A quantum theory of molecular structure and its applications, Chem. Rev. 91 (1991) 893–928, https://doi.org/10.1021/cr00005a013.
[71] U. Koch, P.L.A. Popelier, Characterization of C-H-O hydrogen bonds on the basis of the charge density, J. Phys. Chem. 99 (1995) 9747–9754, https://doi.org/10.1021/j100024a016.
[72] E. Espinosa, E. Molins, C. Lecomte, Hydrogen bond strengths revealed by topological analyses of experimentally observed electron densities, Chem. Phys. Lett. 285 (1998) 170–173, https://doi.org/10.1016/S0009-2614(98)00036-0.
[73] M. Udayakumar, M. Cerón, P. Ceballos, M.J. Percino, S. Thamotharan, Correlation between structural and optical properties of π-conjugated acrylonitrile derivatives: insights from X-ray, energy frameworks, TD-DFT and charge density analysis, J. Mol. Struct. 1213 (2020), 128174, https://doi.org/10.1016/j.molstruc.2020.128174.